Journal of Applied Fluid Mechanics, Vol. 17, No. 8, pp. 1774-1791, 2024.
Available online at www.jafmonline.net, ISSN 1735-3572, EISSN 1735-3645.
https://doi.org/10.47176/jafm.17.8.2293

Numerical Investigation of Vortex Generator on Controlling Flow Field of Centrifugal Pump Based on Response Surface Method

N. Qiu†, M. Li, J. Wu, H. Zhu and P. Xu

Research Center of Fluid Machinery Engineering and Technology, Jiangsu University, Zhenjiang, 212013, China

†Corresponding Author Email: qiuning@ujs.edu.cn

ABSTRACT

The performance and life of centrifugal pumps can be severely impacted by cavitation. In this study, a vortex generator was placed on the blades of the first-stage impeller of a BB4 multistage centrifugal pump to investigate its effect on the local flow field. The response surface method was employed to design various solutions based on the vortex generator's arrangement position, height, and rotation angle and the optimum parameters were φ = 20°, θ = 10°, and h = 1.2114 mm. The results showed that a pressure rise occurred at the corresponding position of the vortex generator, and the pressure variation ranges from 1.99%-8.91%, which is closely related to the height parameter of the vortex generator. In the flow field near the vortex generator, the velocity increased and then decreased along the vertical direction of the blade wall, reaching a maximum height of 1.5 mm. Additionally, the low-velocity zone formed at the end of the vortex generator gradually became larger with the downward movement of the arrangement position, and its velocity varies in the range of about 1.5 m/s-15.7 m/s, and the pressure varies in the range of about 14,000 Pa-125,000 Pa. This research is crucial for understanding the cavitation control principle of vortex generators in centrifugal pumps.

Article History

Received September 12, 2023
Revised February 29, 2024
Accepted March 4, 2024
Available online May 29, 2024

Keywords:

Cavitation
Centrifugal pump
Vortex generator
Response surface method
Cavitation control

1. INTRODUCTION

Cavitation is a prevalent phenomenon in hydraulic machinery, as reported by Yan et al. (2023). This occurs when the local pressure of a liquid falls below its saturation vapor pressure, resulting in the formation of vapor-filled cavities or bubbles within the liquid. These cavities can collapse with a loud noise and generate intense vibrations, as noted by Al-Obaidi (2024). Prolonged operation under cavitation conditions poses severe risks to hydraulic machinery, as highlighted by Zhao et al. (2023).

Response surface methodology (RSM) is an experimental design and analysis method based on mathematical models, which primary purpose is to optimize the effect of multiple factors on a response variable to obtain the optimal response variable value. Many scholars have utilized RSM to investigate the performance of centrifugal pumps. Zhou et al. (2023) investigated the complex interaction between flight height and flow rate on pump performance based on the response surface method, and the results showed that the rotor-stator interaction has a major influence on pressure fluctuation; Cao et al. (2023) considered the number of blades, blade wrap angle, blade outlet angle and other parameters as optimized design variables, and took head and efficiency as response variables, and analyzed 46 sets of hydraulic performance data by using Box-Behnken design method, they found that the optimized model was significantly enhanced in hydraulic performance, and showed significant difference compared with the original model; Qian et al. (2021) established a multivariate regression model based on the response surface method between hydraulic performance of multistage pumps and axial force, the results showed that the blade outlet angle, outlet diameter, and blade wrap angle of the secondary impeller have the greatest influence on the axial force and hydraulic performance of the multistage pump. Wang et al. (2023) investigated the relationship between hydraulic efficiency and the dependent variable within the range of variables using the response surface method, and successfully predicted the performance of hydraulic efficiency.

Due to the severe damage caused by cavitation to the stable operation of hydraulic machinery, extensive research has been conducted to investigate the factors influencing cavitation and methods for its suppression. In their study, Al-Obaidi and Qubian (2022) performed

transient numerical calculations of the flow field in a centrifugal pump with different impeller outlet diameters under different cavitation conditions and demonstrated that the developed model can optimize the pump performance. Bilus and Predin (2009) experimentally investigated the impact of placing diffusers in the inlet pipe on the cavitation performance of centrifugal pumps and found that their use improved the cavitation condition. Zhao and Zhou (2022) studied the influence of adding small blades of varying sizes to the rim of low specific speed centrifugal pump impellers on cavitation erosion and discovered significant inhibition effects in the initial stage of cavitation. Song et al. (2022) conducted numerical simulations to quantitatively analyze the effects of pre-swirl and modified blade profiles on the hydraulic performance and cavitation flow rate of centrifugal pumps, and found that the adopted blade modification method effectively improved the impeller's cavitation performance. Al-Obaidi (2023) used the technique of acoustics to predict cavitation, and the results showed that by using acoustic techniques, detailed information on the results of cavitation detection can be obtained for a variety of conditions. Long et al. (2021) employed a combined experimental and numerical simulation approach to study cavitation flow structures in jet pumps and established a relationship between cavitation and vortex flow. Al-Obaidi (2019) analyzed the results of vibration signals in the time and frequency domains and predicted cavitation in centrifugal pumps, and the results showed that the frequency domain analysis technique of vibration amplitude can predict cavitation in pumps very well.

In order to reduce the adverse effects of cavitation on hydraulic machinery, it is necessary to control cavitation. Passive control is a simple and easy-to-operate control method, so it has been widely studied by scholars at home and abroad. Zhao et al. (2021) studied the control effect and mechanism of blade surface obstacles on blade cavitation through experimental observation and numerical simulation. Kadivar et al. (2018, 2019, 2020a, b) arranged cylindrical and wedge-shaped vortex generators on a hydrofoil, and found that vortex generators could control flow separation on hydrofoils and suppress cavitation. Che et al. (2019a, b, c) arranged micro vortex generators (MVGs) on the surface of a hydrofoil, and found that arranging vortex generators on the leading edge of hydrofoils could change the original finger-like cavitation structure, forming a new type of cavitation structure, thus inhibiting the development of cloud cavitation. Qiu et al. (2020) studied the effect of micro vortex generators arranged on the leading edge of hydrofoils on cavitation erosion, and found that after arranging vortex generators, the cavitation area on hydrofoils was significantly improved. Long et al. (2022) simulated the cavitating flow of propellers by arranging vortex generators on the surface of the ship body, and found that vortex generators could reduce the extremely low-speed region in the wake of the ship body, making the development of cavitation more moderate. Huang et al. (2020) used vortex generators to induce early occurrence of propeller cavitation, and the results showed that vortex generators made the energy distribution of the flow field smoother.

Vortex generator, as a simple and efficient control method, has been widely investigated on hydrofoils, but its engineering application has not been fully investigated. The purpose of this study is to investigate the control effect of the vortex generator on the flow field of a centrifugal pump. The optimal size of the vortex generator is determined by the response surface method, and the effects of different positions of the vortex generator on the flow field of the centrifugal pump are investigated by using numerical calculations.

2. NUMERICAL METHOLOGY

2.1 Numerical Simulation Methods and Verification

The equations employed in this simulation are based on the Navier-Stokes equations (Al-Obaidi & AIhamid 2023). The formulation of the equation is as follows:

$$\frac{\partial \rho_m}{\partial t}+\frac{\partial(\rho_m u_j)}{\partial x_j}=0 \tag{1}$$

$$\frac{\partial(\rho_m u_i)}{\partial t}+\frac{\partial(\rho_m u_i u_j)}{\partial x_j}=-\frac{\partial p}{\partial x_i}+\frac{\partial}{\partial x_j}\times\left[(\mu+\mu_T)\left(\frac{\partial u_i}{\partial x_j}+\frac{\partial u_j}{\partial x_i}-\frac{2}{3}\frac{\partial u_i}{\partial xj}\delta_{ij}\right)\right] \tag{2}$$

Where ρ indicates the density of the fluid, u indicates the fluid velocity, p indicates the ambient pressure, u_t indicates the turbulent viscosity coefficient.

2.2 Cavitation Model

The Zwart model (Yu et al., 2023) is a cavitation model based on mass transport equations, which mainly describes the cavitation phase change process by establishing the transport relationship between gas and liquid phases. The definitions of evaporation rate and condensation rate are as follows:

$$\frac{\partial\left(\rho_v \alpha_v\right)}{\partial t}+\nabla(\rho_v \alpha_v u)=\dot{m} \tag{3}$$

$$\dot{m}^{+}=-C_{dest}\frac{3\alpha_{nuc}(1-\alpha_v)\rho_v}{R_B}\left(\frac{2}{3}\frac{p_v-p}{\rho_l}\right)^{1/2},\ p<p_v \tag{4}$$

$$\dot{m}^{-}=-C_{prod}\frac{3\alpha_v\rho_v}{R_B}\left(\frac{2}{3}\frac{p-p_v}{\rho_l}\right)^{1/2},\ p>p_v \tag{5}$$

Where α_{nuc} indicates the gas core volume fraction, C_{prod} indicates the evaporation coefficient， C_{dest} indicates the condensation coefficient.

2.3 Turbulence Model

The SST k-w turbulence model (Cheng et al., 2023) was used in this simulation. The SST k-w turbulence model is a hybrid model based on the standard k-ε turbulence model and the k-w turbulence model. It can automatically switch to the k-w turbulence model in the near-wall region to capture the details of the flow field in the near-wall region, while the standard k-ε turbulence model was used in the region farther from the wall. In

addition, the transfer of turbulent shear stresses was considered in the turbulent viscosity, which makes the SST k-w model more accurate and reliable than the standard k-ε model. It is suitable for the calculation of internal flow field, separated flow and jet, exhibiting higher precision in capturing the distribution of pressure and velocity gradients, and its equation expression are as follows:

$$\frac{\partial(\rho k)}{\partial t}+\frac{\partial}{\partial x_j}\left(\rho U_j k\right)= \frac{\partial}{\partial x_j}\left[\left(\mu+\frac{\mu_t}{\sigma_k}\right)\frac{\partial k}{\partial x_j}\right]+P_k-\beta^*\rho k\omega \tag{6}$$

$$\frac{\partial(\rho\omega)}{\partial t}+\frac{\partial}{\partial x_j}\left(\rho U_j\omega\right)=\frac{\partial}{\partial x_j}\left[\left(\mu+\frac{\mu_t}{\sigma_\omega}\right)\frac{\partial\omega}{\partial x_j}\right] +\alpha\frac{\omega}{k}P_k-\beta\rho\omega^2+2\left(1-F_1\right)\rho\frac{1}{\sigma_{\omega 2}\omega}\frac{\partial k}{\partial x_j}\frac{\partial\omega}{\partial x_j} \tag{7}$$

$$\mu_t=\frac{a_1 k}{max\left(a_1,\omega,SF_2\right)} \tag{8}$$

Where P_k indicates the turbulent production rate, and S indicates the estimated strain rate.

2.4 Pump Parameters

The research conducted in this study focuses on the BB4 type multistage centrifugal pump, with the first-stage impeller selected as the research object. The three-dimensional structure of the pump under investigation is illustrated in Fig. 1, and the impeller parameters are showed in Table 1.

2.5 Grid Setup and Boundary Condition

ICEM software was used for this simulation to generate a hexahedral structured mesh for the computational domain, and the mesh refinement was applied on key areas such as the blade surface and vgs by

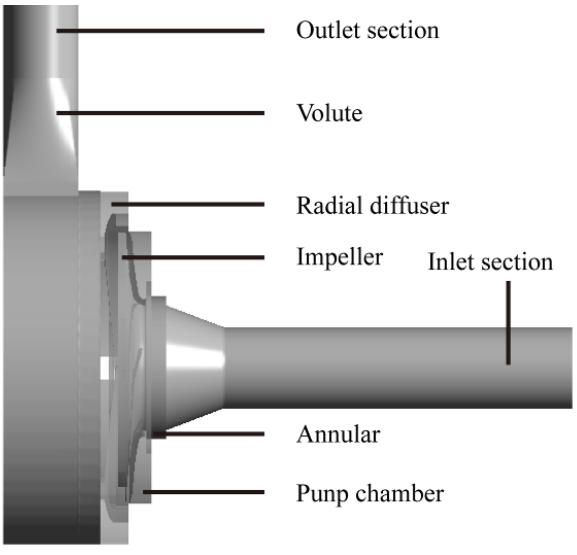

Fig. 1 Centrifugal pump full flow field three-dimensional structure

Table 1 First stage impeller structure parameters

Parameter	Value	Parameter	Value
Number of blades(z)	5	Impeller inlet diameter (D_j)	108 mm
Specific Speed(n_s)	41.65	Impeller diameter (D_2)	233 mm
Inlet pipe diameter (Ds)	80mm	Impeller outlet width (b_2)	6.4 mm
Outlet pipe diameter (D_d)	96mm	Blade wrap angle (β)	136.4°

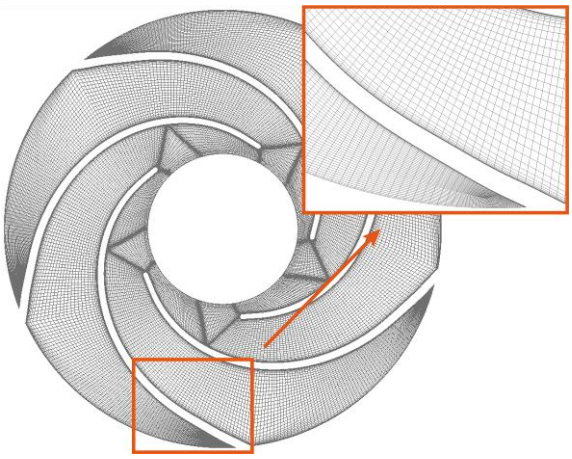

Fig. 2 Grid details

Fig. 3 Distribution of Y+ on the blade surface

adjusting the number of nodes as well as the height of the first layer of the mesh, and the mesh details are shown in Fig. 2. The range of blade Y+ is from 1 to 30, which fits the computational requirements of the turbulence model, and the distribution of blade Y+ is shown in Fig. 3. CFX 19.2 software was used to perform Computational Fluid Dynamics (CFD) simulations (Cao et al., 2022), with the wall set to No slip wall, the inlet set to Pressure inlet with a value of 1 atm, and the outlet set to Flow outlet (36m^3/h). The impeller was modeled as a rotating domain with a speed of 3800 r/min, while other parts were treated as stationary domains. The dynamic-static interface method was employed to couple the impeller with the pump chamber and volute, and the static-static interface method was used to couple the remaining interfaces. A separation

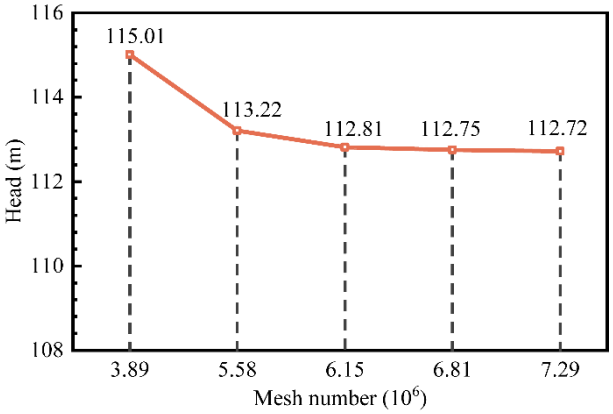

Fig. 4 Grid-independent verification

solver was used to couple the pressure-velocity scheme, and the second-order upwind scheme was used to discretization the difference equations. The turbulent kinetic energy term and the turbulent energy dissipation rate term were solved using the high resolution scheme, and the near-wall flow was approximated using the standard wall function method, and the convergence accuracy set to 10^{-5}.

2.6 Grid Independence Verification

Numerical simulations are subject to various factors that can affect the accuracy of the results, such as grid size and quantity. Therefore, it is crucial to conduct grid independence verification. In this study, the rated operating condition was selected for verification, with head variation serving as the criterion for grid suitability. The verification results are presented in Fig. 4, which shows that the head decreases initially and stabilizes gradually as the number of grids increases. After considering both the calculation accuracy and computational resource limitations, a grid scheme of 6.15×10^6 cells was ultimately chosen for the final numerical simulation.

3. Study of Response Surfaces of Vortex Generator

3.1 Vortex Generator Parameter Design

Vortex generators are devices that generate strong vortices in a fluid to modify the flow field. The shape and size of vortex generators directly affect the generation mode and intensity of the vortices. Generally, it is recommended to match the shape and size of vortex generators with the controlled equipment to achieve optimal flow control effects.

The size design of the vortex generator is based on reference (Qiu et al., 2020), and its structure is depicted in Fig. 5. The side of the vortex generator is perpendicular to the blade surface, with the length of the bottom edge set as l, the length of the leading edge as z, the relative height as h_{vg}, and the thickness as w. The angle between the incoming flow direction and the side surface of the vortex generator is defined as θ. Due to the counter-rotation arrangement of the vortex generators, they exhibit a paired characteristic, where two individual vortex generators form a pair. The minimum distance between the two vortex generators is set as "m", and the maximum distance is set as λ.

The height h of the vortex generator, the counter-rotation angle θ, and the relative position arrangement of the vortex generator are key parameters that affect its role in flow control. In hydrofoil research, the chordwise position of the vortex generators on the hydrofoil is used as a quantitative criterion for their arrangement. Taking into account the twist characteristics of centrifugal pump blades, this study defines the angle φ between the placement position of the vortex generator and the leading edge of the blade as a position parameter. The specific arrangement scheme of the vortex generator is shown in Fig. 6. As the angle φ increases, the relative position of the vortex generator also changes accordingly.

3.2 Response Surface Analysis of Vortex Generator Design Parameters

In this study, a Box-Behnken design with three factors and three levels was utilized for the experimental design. The factors included the placement parameter φ of the vortex generators (coded as X_1), the counter-rotation angle θ of the vortex generators (coded as X_2), and the height h of the vortex generators (coded as X_3). The specific parameters of the experimental design are presented in Table 2. It is important to note that the vortex generators used in this study had a triangular wing shape rather than a right-angled triangle form, so the height h was used to represent the specific height of the vortex generators. Figure 7 illustrates the design schemes for

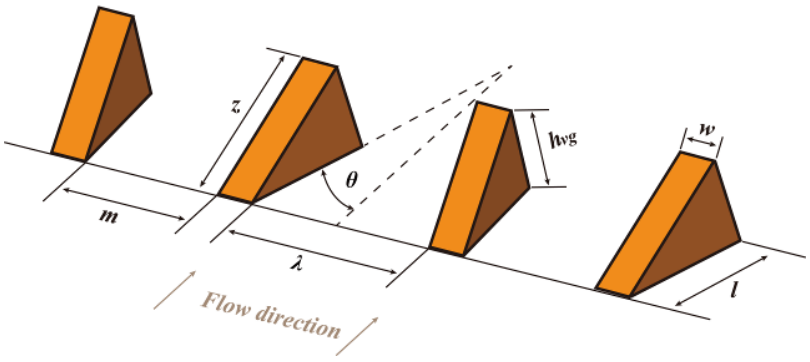

Fig. 5 Structure design of vortex generators

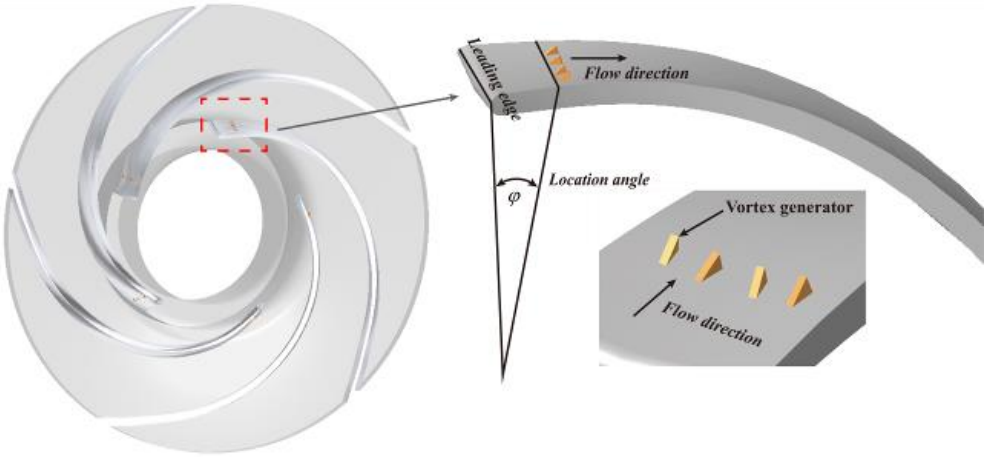

Fig. 6 Layout position of vortex generators

Table 2 Test parameters (three factors - three levels)

Factor	Parameter	Level		
		-1	0	1
X_1	φ/°	10	20	30
X_2	θ/°	5	10	15
X_3	h/mm	0.9157	1.2114	1.4464

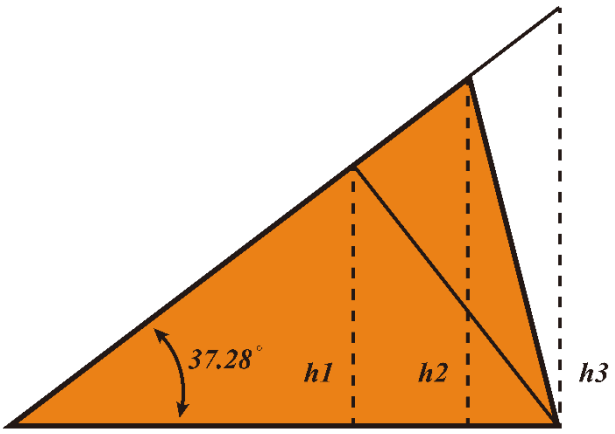

Fig. 7 Height design of vortex generators

three different vortex generator heights. Due to the multiple options for height h and counter-rotation angle θ, the structural dimensions of the vortex generators varied accordingly. The detailed structural parameters are listed in Table 3.

Table 3 Structure design parameters of vortex generators

l/mm	z/mm	h/mm	w/mm	m/mm	λ/mm	θ/°
1.9	1.5118	0.9157	0.5	2	2.3312	5
1.9	2.0000	1.2114	0.5	2	2.6599	10
1.9	2.3879	1.4464	0.5	2	2.9835	15

To evaluate the effectiveness of various vortex generator placement schemes in controlling the cavitation flow field of a centrifugal pump, 13 different arrangements were designed and 17 sets of cavitation simulations were conducted. To compare the cavitation performance of different schemes under the same inlet pressure conditions, the vapor volume in the impeller passage was used as an evaluation metric. The vapor volume effectively reflects the cavitation development status of the pump. In this study, the vapor volume at an inlet pressure of 0.3 atm was chosen as a quantitative evaluation parameter to assess the cavitation control effects of different arrangement schemes.

After completing the numerical calculations, a variance analysis was conducted on the vapor volume, and the results are presented in Table 4. The F-value of the regression model is 81, with a P-value less than 0.0001 (P-value should be less than 0.05), indicating the significance of the model. The coefficient of determination (R^2) of the regression equation is 0.9905, indicating that the model can explain 99.05% of the variation in the vapor volume (Y). Additionally, the adjusted R^2 is 0.9783 and the predicted R^2 is 0.8916, with a difference of less than 0.2 between them. This suggests a high degree of fit between the predicted and actual values, indicating the feasibility of the established model. It is important to note that the P-value for lack of fit should be greater than 0.05 to demonstrate the absence of a significant lack of fit in the regression model. In this study, the P-value for lack of fit is 0.1666, significantly greater than 0.05, indicating that the regression model does not exhibit a significant lack of fit and that the experimental errors are small, thus demonstrating a high level of reliability.

In the analysis of variance presented in Table 4, the corresponding P-values reflect the significance of the effects. If the P-value is less than 0.05, it indicates a significant effect. The closer the P-value is to 0, the more significant the effect. When the P-value is greater than 0.05, it suggests that the effect is not significant and is considered a weak factor. Based on the analysis of variance table, the following conclusions can be drawn: the position parameter (X_1) is a strongly significant factor, while the angle of attack (X_2) and VG height (X_3) are

Table 4 Analysis of variance

Source	Sum of Squares	df	Mean Square	F-value	P-value	
Model	8.84	9	0.982	81	< 0.0001	significant
X_1	0.3214	1	0.3214	26.51	0.0013	
X_2	0.0168	1	0.0168	1.39	0.2771	
X_3	0.0041	1	0.0041	0.3361	0.5803	
X_1X_2	0.0907	1	0.0907	7.48	0.0291	
X_1X_3	0.1216	1	0.1216	10.03	0.0158	
X_2X_3	0.0014	1	0.0014	0.1187	0.7406	
X_1^2	6.85	1	6.85	564.93	< 0.0001	
X_2^2	0.0245	1	0.0245	2.02	0.1984	
X_3^2	1.03	1	1.03	85.25	< 0.0001	
Residual	0.0849	7	0.0121			
Lack of Fit	0.058	3	0.0193	2.88	0.1666	not significant
Pure Error	0.0269	4	0.0067			
Cor Total	8.92	16	R^2	0.9905		
Std. Dev.	0.1101		Adjusted R^2	0.9783		
Mean	19.87		Predicted R^2	0.8916		
C.V. %	0.5541		Adeq Precision	25.1312		

weakly significant factors. Additionally, the order of the effects is X_1 (0.0013) > X_2 (0.2771) > X_3 (0.5803).

After regression analysis, the final regression equation obtained is as follows:

$$Y=18.99+0.2011X_1+0.046X_2+0.0226X_3-0.1506X_1X_2-0.1738X_1X_3+0.0189X_2X_3+1.28X_{12}+0.0762X_{22}+0.5037X_{32}$$

To visually illustrate the impact of placement position, angle of attack, height, and their interactions on bubble volume, three-dimensional response surfaces and two-dimensional contour were plotted as shown in Fig. 8. As seen in Fig. 8(a), the placement position has a more significant effect on bubble volume compared to the angle of attack. Within the given range, the optimal placement position φ is between 18° and 20°，while the optimal angle of attack θ is between 5° and 11°. Figure 8(b) demonstrates that the placement position has a greater influence on bubble volume than VG height. The optimal VG height h is between 1.13 mm and 1.23 mm. Figure 8(c) reveals that VG height has a more pronounced effect on bubble volume than the angle of attack. Therefore, the optimal experimental configuration is to conduct the study with parameters φ = 20°, θ = 10°, and h = 1.2114 mm.

In conclusion, it can be concluded that the placement position of VGs has the greatest impact on bubble volume, followed by VG height, while the angle of attack has the least influence. This suggests that the rotational arrangement of VGs has limited control over the flow field in a centrifugal pump, but the placement position of VGs remains the most crucial factor in controlling the flow field.

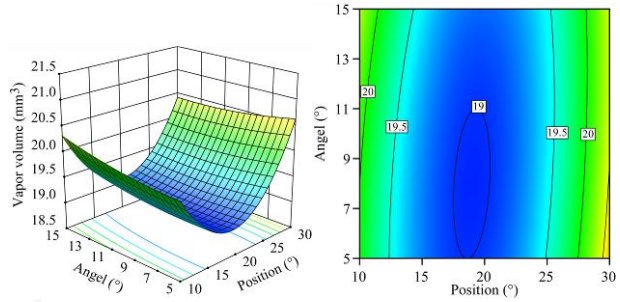

(a) Effects of position and pitch angle on cavitation

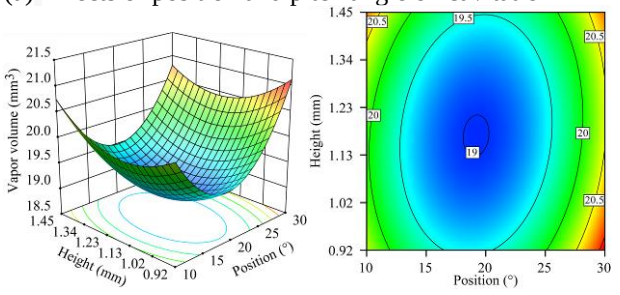

(b) Effects of height and position on cavitation

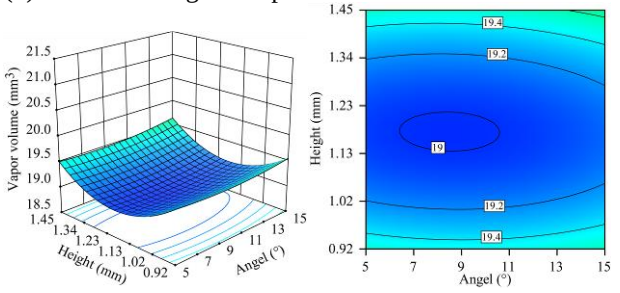

(c) Effects of height and pitch angle on cavitation

Fig. 8 Effect of interaction of influence factors on vapor volume

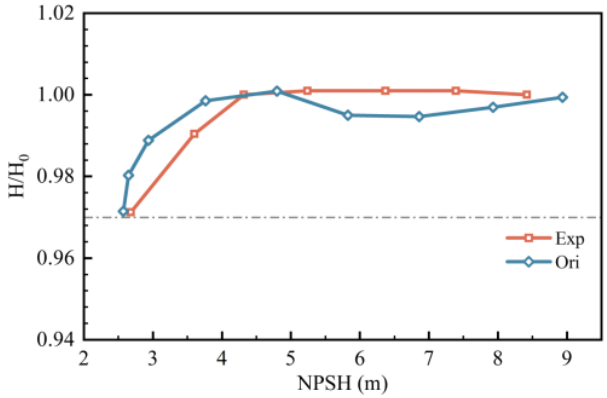

Fig. 9 Comparison of experiment and simulation verification

Table 5 Parameters of VGs Scheme

Program	Position	Height *h*/mm	Angle *θ*/°
1	1	0.9157	10
2	1	1.4464	10
3	2	1.2114	10
4	2	1.4464	5
5	2	1.4464	10
6	2	1.4464	15
7	3	0.9157	10
8	3	1.4464	10

4. RESULTS AND DISCUSSION

4.1 Experimental Verification

Figure 9 compares the experimental and simulated results for cavitation performance verification. As seen from the graph, as the NPSH decreases, the experimental curve remains relatively constant in terms of head initially. However, when the NPSH decreases to approximately 4.5m, the head starts to decline slowly. A further reduction to 2.6m results in a 3% decrease in head, which is considered the critical cavitation point. The simulated curve initially shows some pressure fluctuations during the cavitation pressure reduction calculation, indicating that the initial cavitation flow field is influenced by variations in inlet pressure and lacks stability. However, as the inlet pressure continues to decrease, the flow field gradually becomes more stable and follows a predictable pattern. The simulated curve aligns well with the experimental results, particularly at the critical point, suggesting that the simulation results are reliable.

4.2 Pressure-Velocity Characteristics Around Vortex Generators

The effect of vortex generator (VG) on cavitation volume in centrifugal pumps was investigated by response surface analysis. The results of the study showed that placement position is the most significant factor, followed by VG height, while swirl angle has a relatively minor impact. Before analyzing cavitation, it is crucial to study the local influence of the vortex generator on non-cavitating flow fields. Several schemes were chosen for comparison, as listed in Table 5. In order to clearly describe the placement of the VGs, they are named positions 1, 2 and 3, corresponding to angles of 10°, 20° and 30°, respectively.

Figure 10 compares the surface pressure distribution at the spanwise location of Span=0.5 on a typical blade for different schemes. It is obvious that there is an increase in pressure at the placement position of the vortex generator, followed by a rapid decrease and a return to normal levels, and the pressure variation ranges from 1.99%-8.91%, indicating that the vortex generator only affects the local area's pressure distribution. Comparing Scheme 1 and Scheme 2, it can be found that due to the higher height of the vortex generator in Scheme 2, the disturbance in the local area is more significant, resulting in larger pressure variations. Furthermore, comparing Scheme 4, 5, and 6, it can be found that the scheme with a swirl angle of 5° exhibits minimal pressure change, while the scheme with a swirl angle of 10° is slightly higher than the scheme with a swirl angle of 15°. It is worth noting that for the first two schemes with forward placement positions, the pressure at the front end of the vortex generator is higher, especially in Placement 2. However, for Placement 3, the pressure at the front end of the vortex generator remains consistent with the original blade's pressure, with an increase in pressure occurring only after encountering the disturbance from the vortex generator, followed by a decrease to a level lower than that of the original blade. Considering the overall pressure change process, the presence of the vortex generator leads to a relatively small increase in pressure compared to the original blade's pressure distribution, primarily due to the influence of pressure decrease. Therefore, it can be inferred that the vortex generator alters the local flow field, hindering fluid flow near the blade surface, and resulting in a localized increase in pressure at the front edge of the vortex generator. Downstream of the vortex generator, the pressure quickly returns to normal levels or even slightly lower than without the vortex generator.

Based on the above analysis, it can be concluded that vortex generators have an impact on the local flow field. To better understand this impact, line segments were drawn at four positions before and after the vortex generators on the Span=0.5 section of a typical blade. Each line segment was 5 mm long and perpendicular to the blade surface, labeled as Line 1 to Line 4, as shown in Fig. 11. The velocities along these four lines segments were extracted and presented in Fig. 12. From the figure, it is obvious that significant velocity variations occur within the boundary layer close to the blade surface, with the magnitude of velocity changes decreasing as the height increases. By comparing Scheme 1 and Scheme 2, it is observed that Scheme 2, which has a higher height of the vortex generator, exhibits larger velocity differences before and after the vortex generator, indicating significant flow field variations. Furthermore, when comparing Scheme 4, Scheme 5, and Scheme 6, it is found that these three schemes show a similar trend in velocity changes, indicating that the variation in velocity along the extraction lines is less affected by the swirl angle. Further examination of the velocity profiles along the extraction lines reveals that they do not follow a consistent pattern but intersect at certain positions. By comparing Scheme 2,

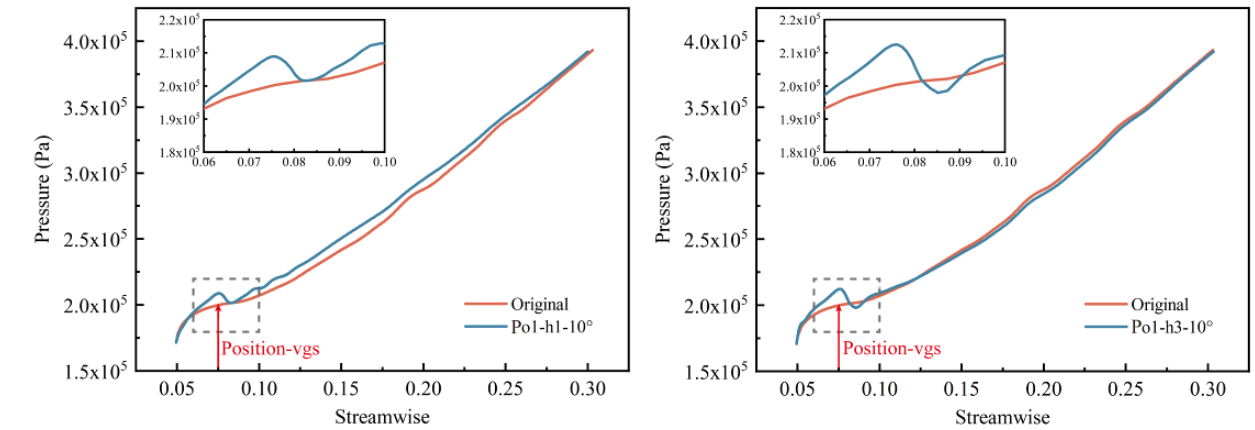

(a)scheme1

(b)scheme2

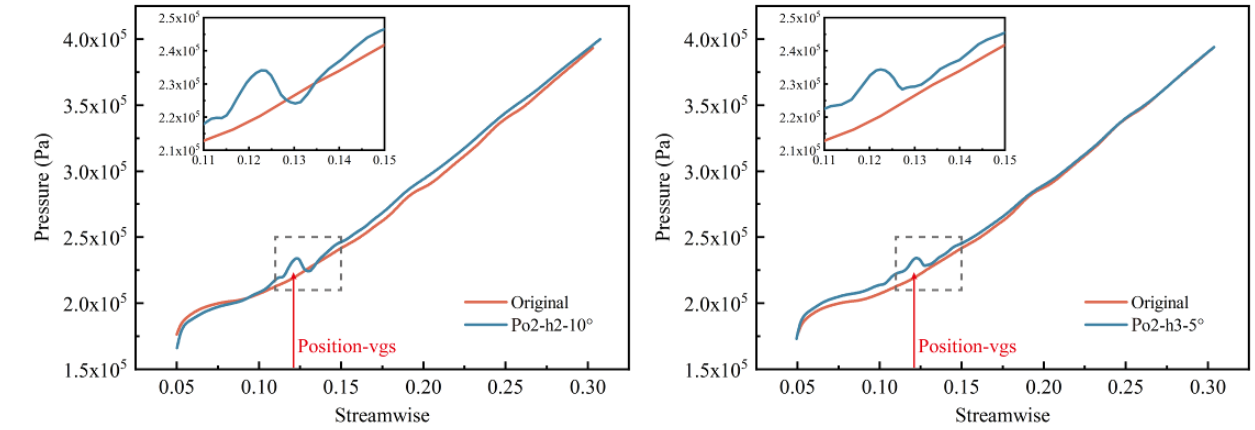

(c)scheme3

(d)scheme4

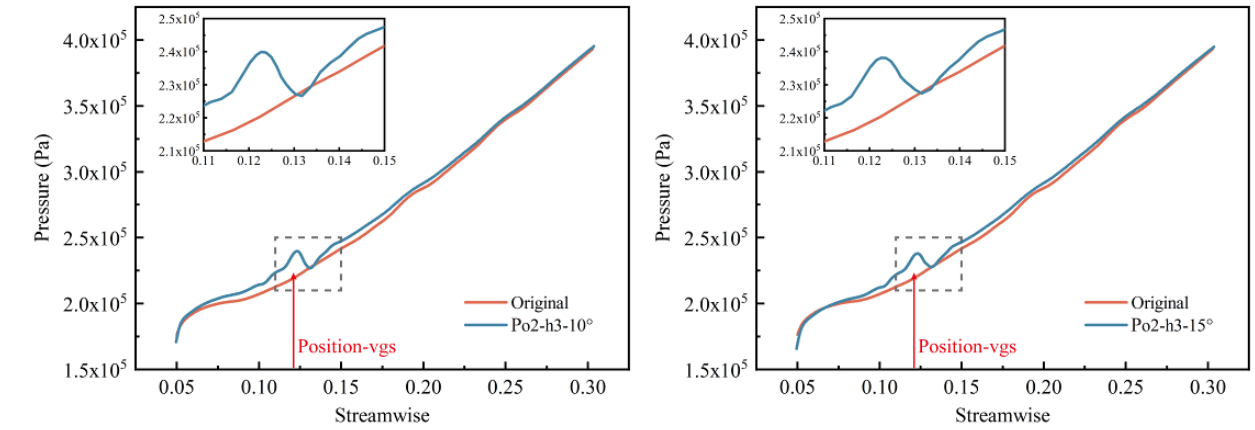

(e)scheme5

(f)scheme6

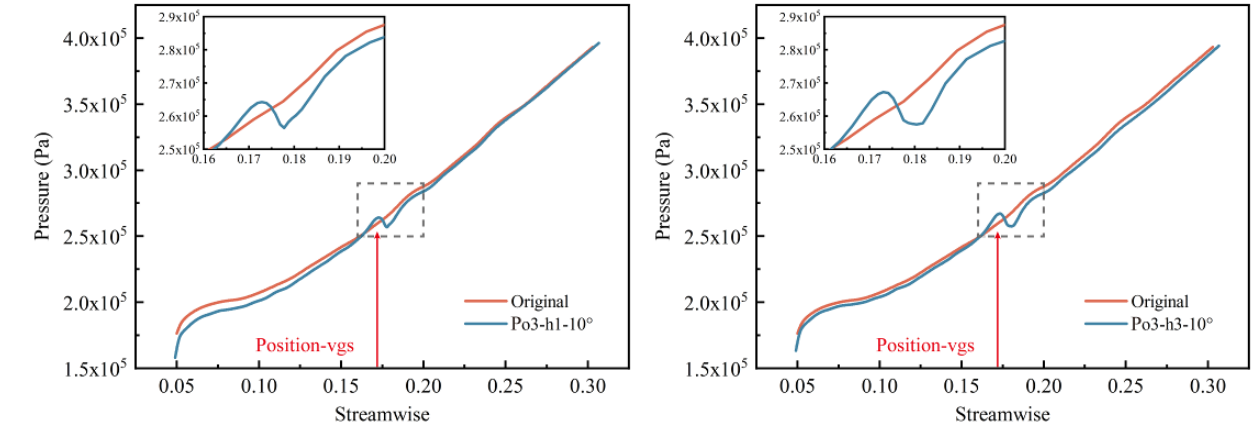

(g)scheme7

(h)scheme8

Fig. 10 Comparison of pressure distribution on typical blade surfaces

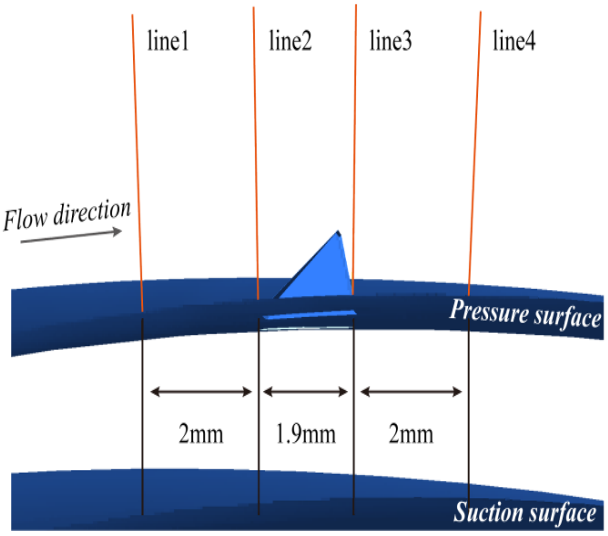

Fig. 11 Extraction line position

Scheme 5, and Scheme 8, it is observed that Scheme 2, which has the most forward placement position, exhibits the largest distance between the velocity intersection point and the blade wall, approximately 4.5 mm. Furthermore, it can be observed that the distance between the velocity. Furthermore, it can be observed that the distance between the velocity intersection point and the blade wall decreases as the placement position moves toward the rear of the blade. Scheme 5 and Scheme 8 have distances of approximately 2.5 mm and 1.8 mm, respectively.

Comparing different placement schemes, it was found that the trend of velocity variation remains consistent within the range of vortex generator heights. It is also worth noting that when the distance between the extraction line and the wall reaches approximately 1.5 mm, the velocity along the extraction line reaches its maximum value before gradually decreasing. Additionally, as the placement position of the vortex generator moves away from the leading edge of the blade, the decreasing trend in velocity becomes more pronounced. Using Line 4 as a reference, when the height of the extraction line is 5 mm, the velocities for Scheme 2, Scheme 5, and Scheme 8 are 14.45 m/s, 12.70 m/s, and 11.57 m/s, respectively.

4.3 Analysis of Downstream Flow Field with Vortex Generators

The placement of vortex generators exhibits a counter-rotating pattern, which can alter the flow conditions in the local region and induce the generation of vortices downstream of the VGs. To gain further insight into the flow characteristics in the downstream region of the VGs, a specific section was selected for analysis at a distance of 3 mm from the trailing edge of the VGs. This section is perpendicular to the blade surface, as illustrated in Fig. 13.

Figure 14 illustrates the velocity distribution at the downstream of the VGs. From the figure, it can be observed that the low velocity regions are generated at specific locations and exhibit counter-rotation corresponding to the location of VGs. In Fig. 14(a), it can be observed that the low-velocity region corresponding to the VGs is small, without a distinct rotational area, whereas in Scheme 2 in Fig. 14(b), the low-velocity region is obvious at the top position and exhibiting characteristic rotational features. This comparison indicates that VGs of different heights form different effects on the flow field near the blades, and the higher height scheme are more significant. Further comparison of Figs. 14(d), (e), and (f) reveals that the area of the low-speed region of scheme 4 in Fig. 14(d) is significantly smaller than that of the other two schemes, while the areas of the low-speed regions of scheme 5 and scheme 6 are basically similar. This indicates that there is a difference in the effect on the flow field between a contra-rotation angle of 5° and contra-rotation angles of 10° and 15°, and that the increase in the contra-rotation angle enhances the effect, but not always with the increase in the contra-rotation angle. Figure 14 (b), (e), and (h) correspond to the location 1, 2, and 3 of the VGs, respectively, the arrangement position is gradually away from the leading edge of the blade. After being obstructed by the VGs, the low velocity region was form after the VGs, and the low velocity region corresponding to the VGs gradually increases as the arrangement location gradually moves downstream of the blade. The region with the smallest velocity in the figure occurs in scheme 7 and at about 1.5 m/s; the region with the largest velocity occurs in scheme 1 and at about 15.7 m/s. It should also be noted that a large flow velocity region was existed at the top of the cross-section, which gradually decreases as the location moves downstream. This is due to the fact that the cross-section position is further away from the leading edge, which is subject to less inlet perturbation and more uniform flow. Under the rotating action of the centrifugal pump, the location of the high velocity region is closer to the area of the impeller hub, and its flow state is shown by the black dashed arrow in Fig. 14(b).

Figure 15 shows the pressure distribution at the downstream of the VGs. As can be seen from the figure, the low-pressure zone arises behind the VGs and exhibit counter-rotation corresponding to the location of VGs. Comparing Fig.15(a) and (b), it can be seen that the pressure corresponding to the rear of the VGs in Scheme 1 is smaller, indicating that different heights of the VGs form different effects on the pressure distribution near the blade. Further comparison of Figs. 15(d), (e), and (f) reveals that the area of the low-pressure region of scheme 4 in Fig. 15(d) is significantly smaller than that of the other two schemes, which indicates that there is a difference in the effect of different counter-rotation angle on the pressure distribution of the flow field. Figure15(b), (e), and (h) correspond to the location 1, 2, and 3 of the VGs, respectively, and the arrangement positions are gradually away from the leading edge of the blade. The low-pressure region corresponding to the VG gradually increases as the arrangement position moves downstream of the blade, indicating that the influence of the arrangement position near the downstream on the pressure distribution is more noticeable. The region of lowest pressure in the figure occurs in scheme 6 at about 14,000 Pa; the region of highest velocity occurs in scheme 2 at about 125,000 Pa.

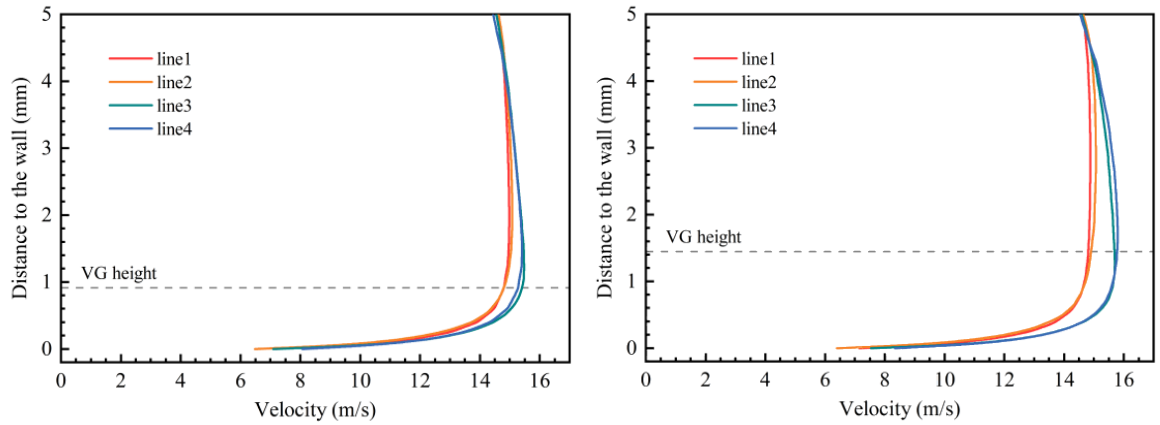

(a)scheme1 (b)scheme2

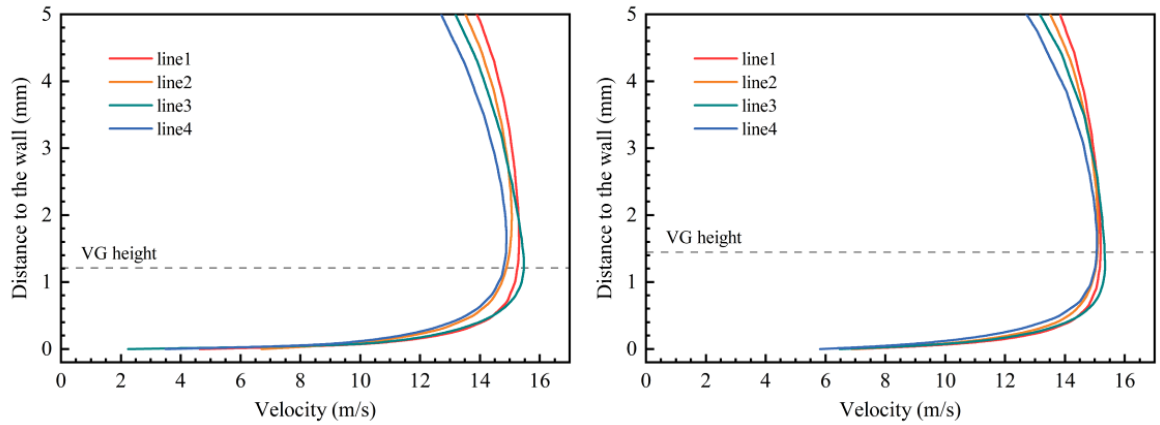

(c)scheme3 (d)scheme4

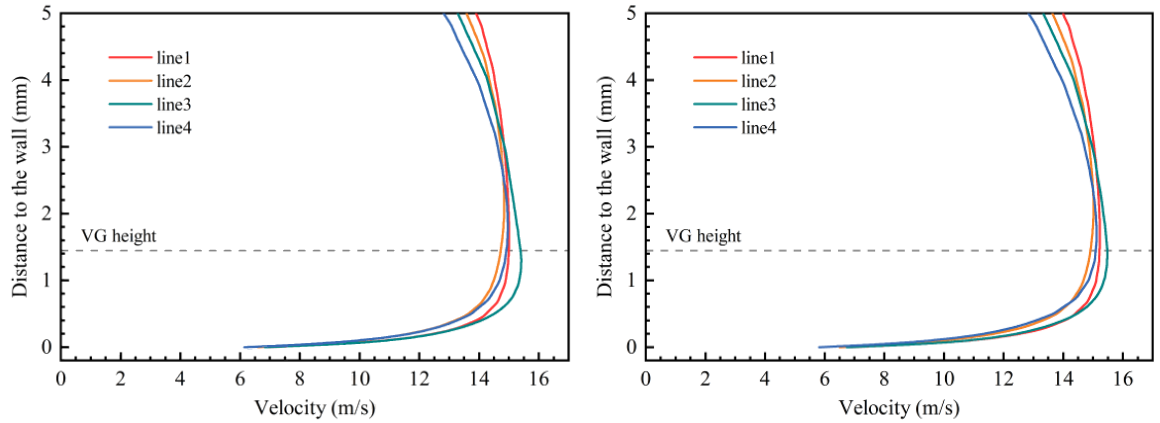

(e)scheme5 (f)scheme6

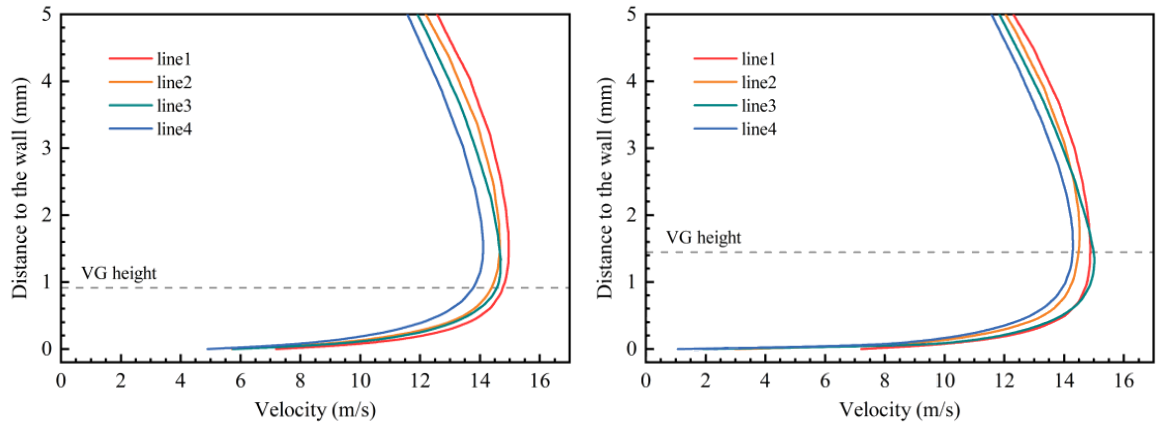

(g)scheme7 (h)scheme8

Fig. 12 Comparison of velocity distribution on typical blade extraction lines

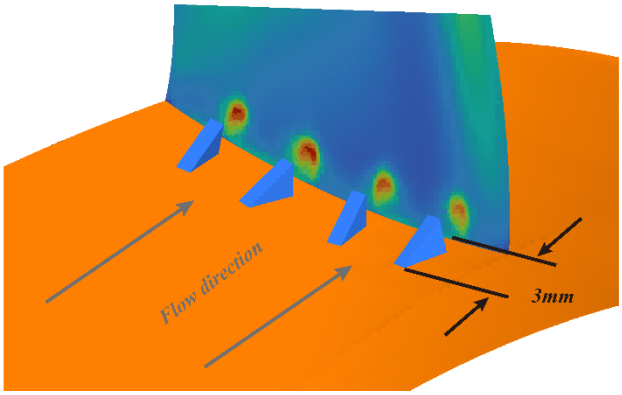

Fig. 13 Position of VGs downstream section

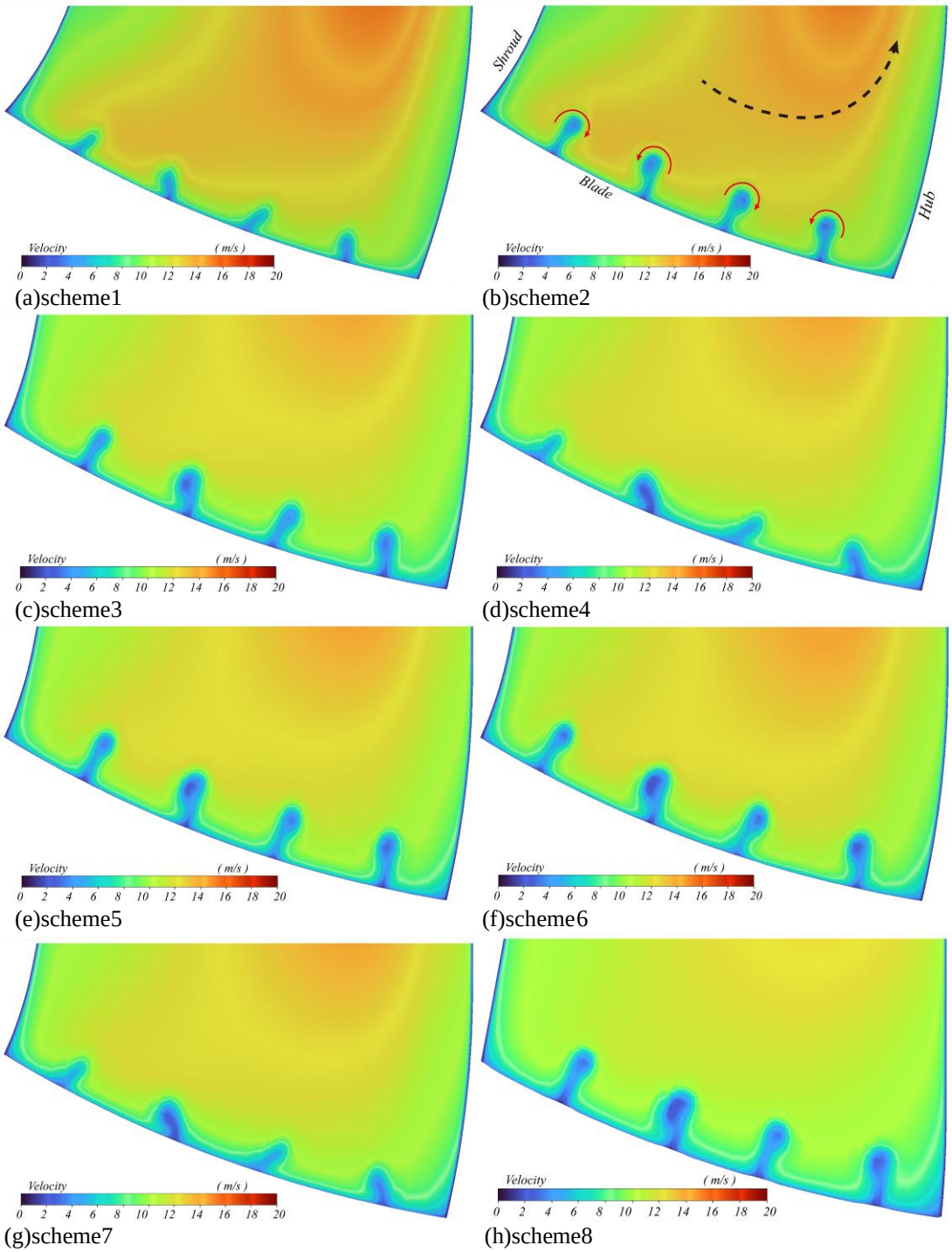

(a)scheme1 (b)scheme2

(c)scheme3 (d)scheme4

(e)scheme5 (f)scheme6

(g)scheme7 (h)scheme8

Fig. 14 Velocity distribution of VGs downstream section

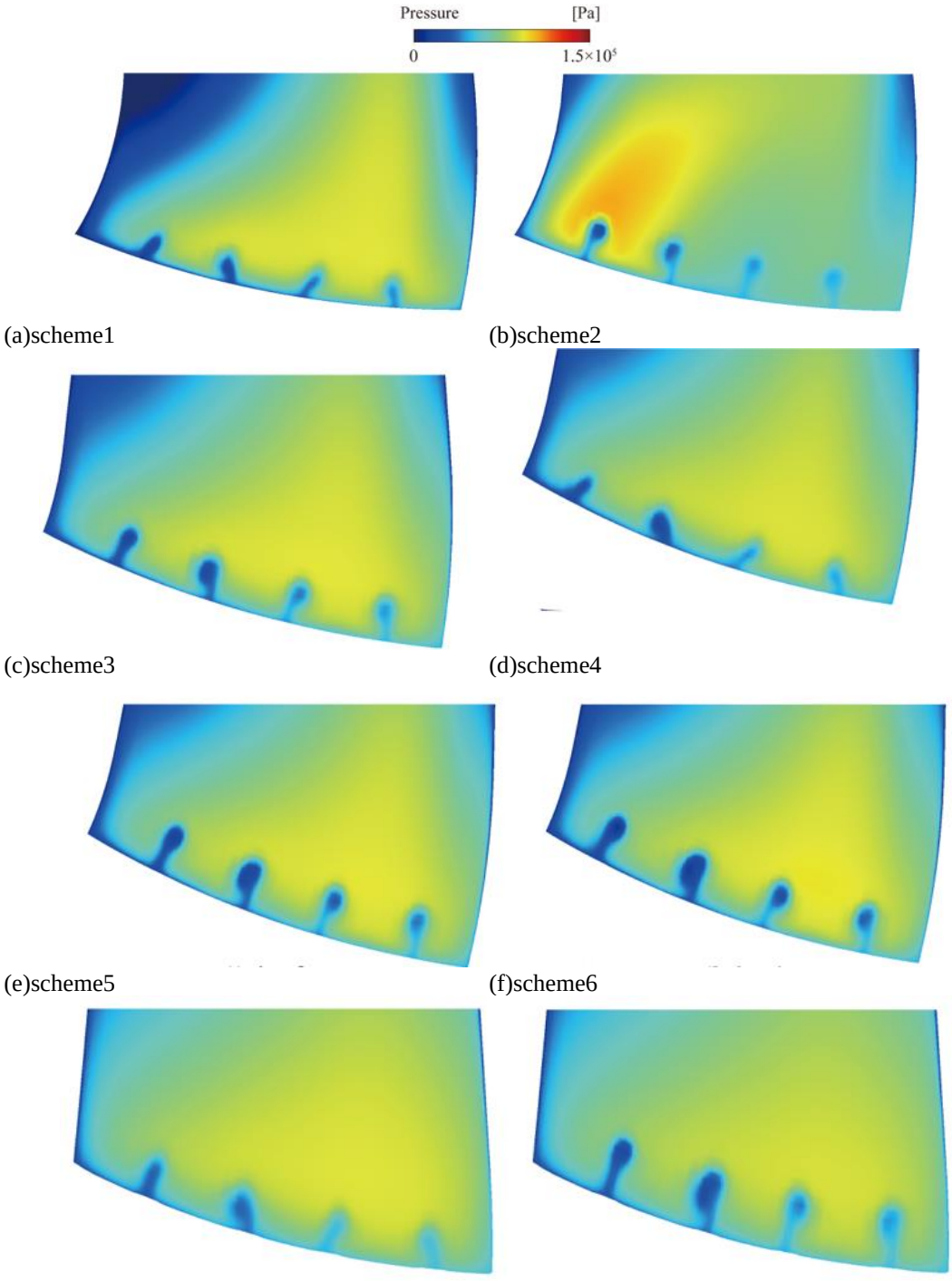

Fig. 15 Pressure distribution of VGs downstream section

Figure 16 presents the vorticity distribution on the downstream section of the VGs based on the Q-criterion. The formula for the Q criterion is shown below (Gu et al., 2023):

$$S = 0.5\left[\frac{\partial u_i}{\partial x_j} + \frac{\partial u_j}{\partial x_i}\right] \tag{9}$$

$$\Omega = 0.5\left[\frac{\partial u_i}{\partial x_j} - \frac{\partial u_j}{\partial x_i}\right] \tag{10}$$

$$Q = 0.5\left[\|\Omega\|_F^2 - \|F\|_F^2\right] \tag{11}$$

From the figure, it can be observed that there are regions of high vorticity intensity corresponding to the VGs' locations, exhibiting a counter-rotating pattern consistent with the arrangement of the VGs. By comparing Figs 16(a) and (b), it is evident that the vorticity distribution in Scheme 2 is more pronounced, whereas Scheme 1 exhibits significantly lower vorticity intensity, indicating that the vortical structures generated by the VGs in Scheme 1 are smaller and have a lesser disturbance

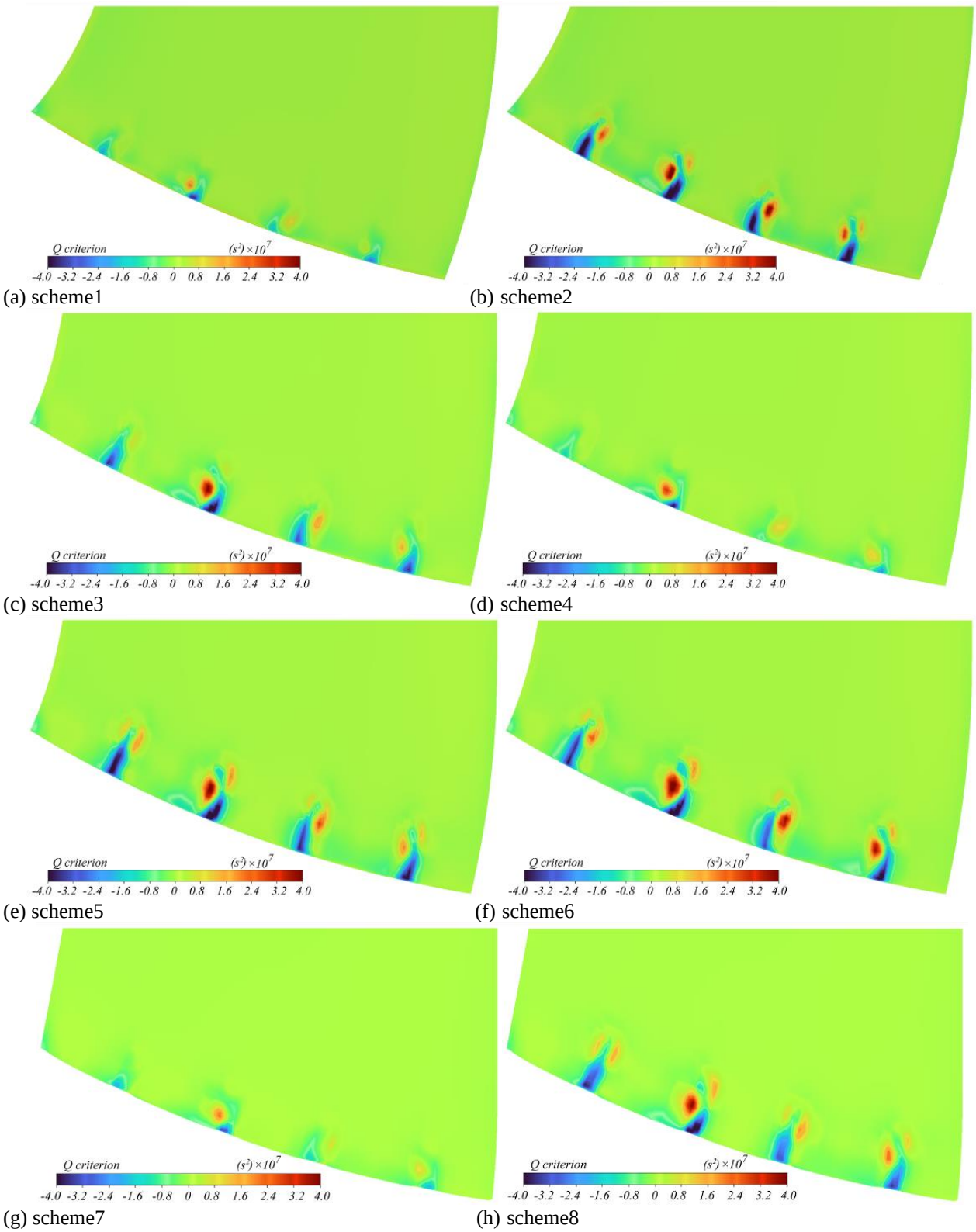

(a) scheme1 (b) scheme2

(c) scheme3 (d) scheme4

(e) scheme5 (f) scheme6

(g) scheme7 (h) scheme8

Fig. 16 Vorticity distribution of VGs downstream section

effect on the flow field. Furthermore, the figure reveals that the outer region of the counter-rotating vorticity distribution consists of negative values, exhibiting a belt-like pattern, which is dominated by the strain rate and exhibits higher values. On the other hand, the inner region consists of positive values and exhibits a cluster-like pattern, which is influenced by the rotational velocity and aligns with the rotating effect of the vortices. By comparing Figus 16(d) and (e), it can be concluded that for the vorticity distribution on the section, the vorticity intensity is significantly lower in Scheme 2 with a counter-rotating angle of 5° compared to Scheme 2 with a counter-rotating angle of 10°, indicating that increasing the counter-rotating angle can significantly enhance the vorticity intensity. This suggests that adjusting the counter-rotating angle of the VGs can be an effective way

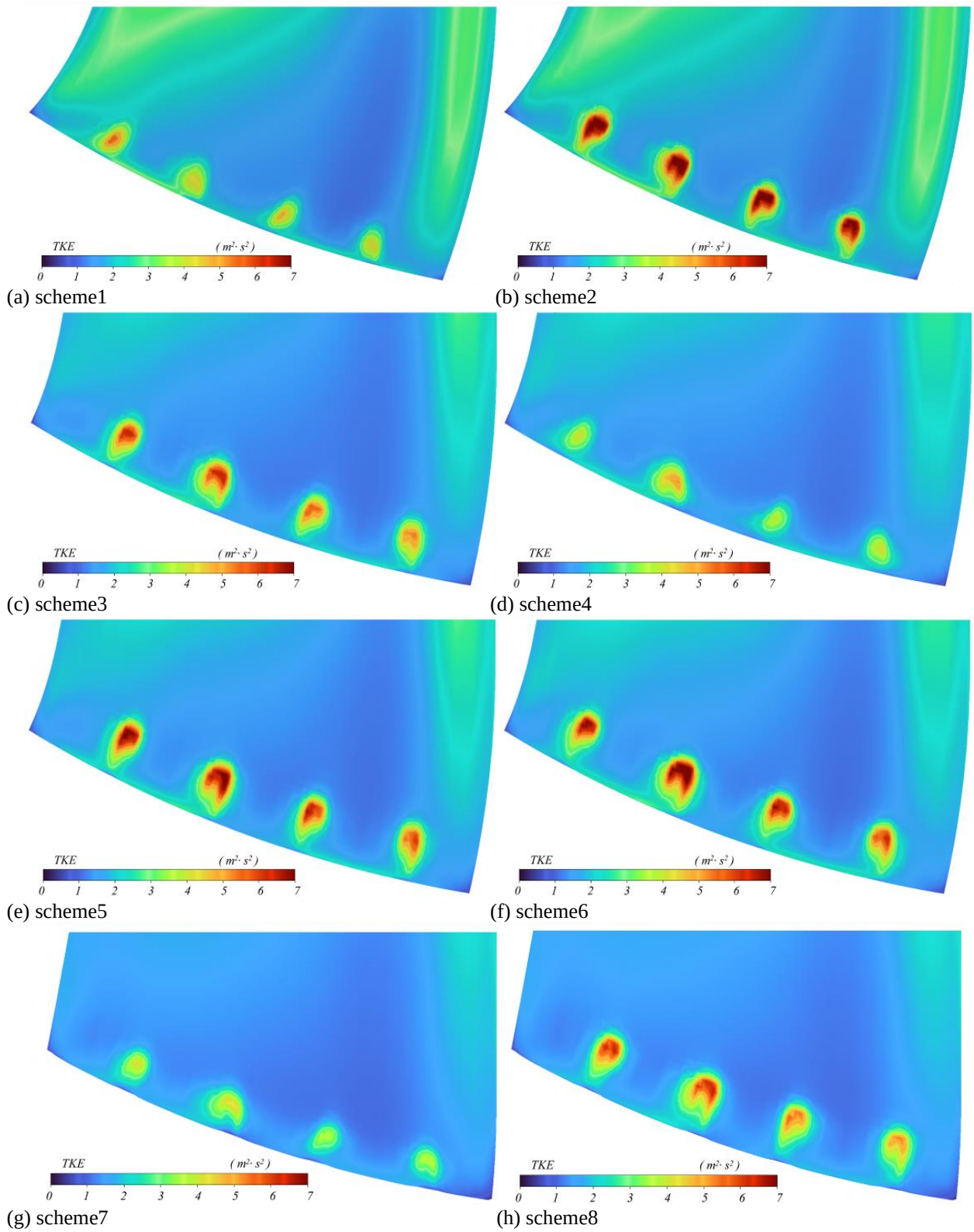

(a) scheme1 (b) scheme2

(c) scheme3 (d) scheme4

(e) scheme5 (f) scheme6

(g) scheme7 (h) scheme8

Fig. 17 Turbulence kinetic energy distribution of VGs downstream section

to control the flow characteristics in their downstream region. However, comparing Figs 16(e) and (f), it is observed that the vorticity intensity does not exhibit a significant increase in Scheme 3 with a counter-rotating angle of 15° compared to Scheme 2 with a counter-rotating angle of 10°. By comparing Schemes 4, 5, and 6, it can be concluded that appropriately increasing the counter-rotating angle of the VGs can enhance the vorticity intensity, but once the counter-rotating angle reaches a certain degree, further increasing the angle results in minimal changes in the vorticity intensity. By comparing Figs 16(b), (e), and (h), it can be observed that the vorticity distribution intensity on the section is similar, indicating that the placement of the VGs has a minor influence on the vorticity. Thus, it can be shown that the vorticity characteristics in the flow field are primarily

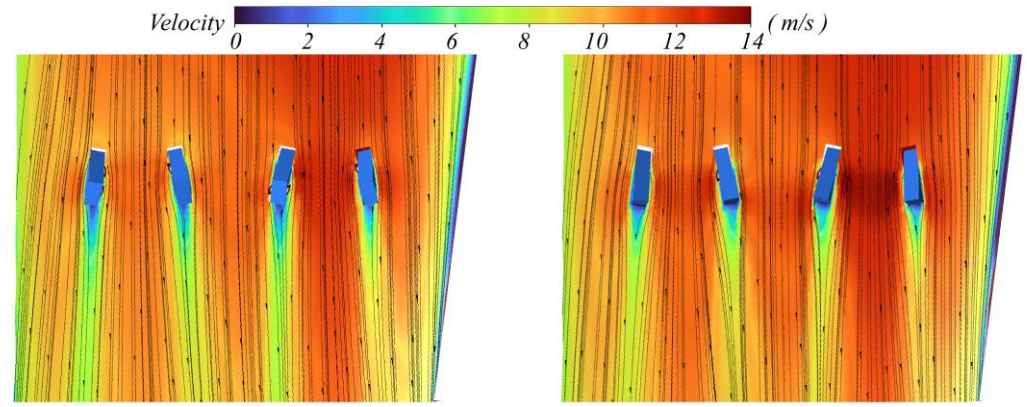

(a) scheme1 (b) scheme2

(c) scheme3 (d) scheme4

(e) scheme5 (f) scheme6

(g) scheme7 (h) scheme8

Fig. 18 Velocity distribution in the middle section of VGs

determined by the morphology and structure of the VGs, while the influence of their placement is relatively minor. Additionally, based on the vorticity distribution, higher vorticity values are observed in the central region, indicating that the VGs in the intermediate spanwise region near the blade's mid-span generate stronger vortical structures and exhibit more significant effects. This suggests that positioning VGs at specific locations along the blade can help optimize their performance and improve their effectiveness in controlling flow separation and enhancing lift generation.

Figure 17 displays the distribution of turbulent kinetic energy on the downstream section of the VGs.

From the figure, it can be observed that there are regions of high turbulent kinetic energy corresponding to the VGs, while the energy intensity near the blade surface is relatively low. The high-energy regions appear in the same locations as the VGs' heights, which differs significantly from the previous analyses of velocity and vorticity distributions. By comparing Figs 17(a) and (b), it can be concluded that the high turbulent kinetic energy region was formed near the high VG. Comparing Figs 17(d), (e), and (f), it is observed that the arrangement with a counter-rotating angle of 5° exhibits the lowest turbulent kinetic energy intensity, while the intensities in the arrangements with angles of 10° and 15° are similar. This finding aligns with the influence of VGs' morphology and dimensions on the vorticity distribution as discussed earlier. Furthermore, there are variations in the turbulent kinetic energy distribution within individual arrangement schemes on the section. By comparing the VGs near the leading and trailing edges, it can be observed that the VGs closer to the leading edge exhibit higher turbulent kinetic energy intensity. By comparing Figs 17(b), (e), and (h), it is observed that as the placement of the VGs moves downstream along the blade, there is a gradual decrease in turbulent kinetic energy on the section. This decrease in intensity is particularly significant in the comparison between location 2 and location 3. Additionally, the turbulent kinetic energy intensity decreases gradually as the VGs' placement moves downstream compared to other sections on the section. This suggests that adjusting the placement of VGs can have a significant impact on their performance and effectiveness in controlling flow separation and enhancing lift generation.

The velocity distribution at 1/2 VG height on the section is presented in Fig. 18. It can be observed from the figure that the high-velocity regions in the section are mainly distributed upstream of the VGs and between adjacent VGs, particularly in the case of arrangement 1 and arrangement 2, where these high-velocity regions are more pronounced. As the fluid passes through the channels between adjacent VGs, the velocity increases due to the narrowing of the flow passage. At the same time, when the fluid flows past the VGs, a noticeable low-velocity region forms at the trailing edge of the VGs due to the obstruction of the flow by the VGs. By comparing Figs 18(a) and (b), it can be found that the low velocity region is smaller in arrangement 2 with higher VG compared to arrangement 1. This is because the lower portion of the VGs in arrangement 2 is closer to the blade surface, resulting in a more pronounced low-velocity region. Comparing Figs (d), (e), and (f), it is observed that the length of the low-velocity region behind the VGs is similar, indicating that the counter-rotating angle has minimal influence on the velocity distribution in the middle section. Furthermore, comparing Figs 18(b), (e), and (h), it can be noted that there are significant differences in the distribution of the low-velocity region among different arrangement schemes. As the placement of the VGs moves downstream, the low-velocity region expands, covering a larger area. Simultaneously, the distribution of higher velocities in the middle section decreases.

5. CONCLUSION

In this study, an in-depth investigation was conducted into the control effect of vortex generators (VGs) on centrifugal pump flow fields. Response surface methods were utilized to examine how the placement, height, and counter-rotating angle of VGs impact cavitation performance. Several representative programs were selected for analyzing flow field characteristics. Based on the findings, the following conclusions can be drawn:

1. Based on the response surface figures of the interaction effects among the parameters of bubble volume, the optimal parameter ranges for three influencing factors were determined. The optimum placement angle φ ranges from 18° to 20°, the counter-rotating angle θ ranges from 5° to 11°， and the height h ranges from 1.13 mm to 1.23 mm. The experimental research plan with parameters φ=20°, θ=10°, and h=1.2114 mm was ultimately determined as the optimal choice.

2. After arranging VGs on the blade surface, blade pressure data was extracted at Span = 0.5. The results showed a noticeable pressure increase at the relative position of VGs, followed by a rapid decrease and return to normal levels, and the pressure variation ranges from 1.99%-8.91%. When comparing the three parameters of VGs, the higher VGs configuration demonstrated a more significant pressure increase effect, with the counter-rotating angle having the most pronounced impact on surface pressure at 10°， and the pressure variation being most prominent at position 2.

3. Four extraction lines were placed before and after the VGs to extract velocities along the lines. The results showed that velocities along the extraction lines increased gradually as the distance from the blade surface increased. However, when the distance reached 1.5 mm, velocities began to decrease gradually. When the height of the extraction line is 5 mm, the velocities for Scheme 2, Scheme 5, and Scheme 8 are 14.45 m/s, 12.70 m/s, and 11.57 m/s, respectively. It is worth noting that velocity variation was particularly significant within the boundary layer.

4. In the study, flow passage sections were arranged downstream of the VGs and vorticity and turbulence kinetic energy distributions were extracted in these sections. The placement of VGs altered the original flow field on the blade surface, forming regions of high vorticity and turbulence kinetic energy at their relative positions. Additionally, a flow passage section was set at the mid-span of the VGs, and velocities and streamlines were extracted in this section. A distinct low-velocity region was observed forming at the trailing edge of the VGs, which became larger as the placement moved downstream, indicating a more significant alteration of the flow field.

ACKNOWLEDGEMENTS

This study is supported by the National Natural Science Foundation of China (No. 51806082), China

Postdoctoral Science Foundation (No. 2020M671363 and No. 2021T140282), Postdoctoral Science Foundation of Jiangsu Province (No. 2020Z298), and Entrepreneurial Doctor Program of Jiangsu Province (No. 18SCBS016).

CONFLICT OF INTEREST

The authors declare that they have no competing interests.

AUTHORS CONTRIBUTION

Ning Qiu: Review and editing. **Minwei Li:** Data collection; Writing original draft. **Jie Wu:** Writing original draft (Supporting). **Han Zhu:** Review and editing. **Pei Xu**: Review and editing.

REFERENCES

Al-Obaidi, A. R. (2019). Investigation of effect of pump rotational speed on performance and detection of cavitation within a centrifugal pump using vibration analysis. *Heliyon*, *5*(6). https://doi.org/10.1016/j.heliyon.2019.e01910

Al-Obaidi, A. R. (2023). Experimental diagnostic of cavitation flow in the centrifugal pump under various impeller speeds based on acoustic analysis method. *Archives of Acoustics*, *48*(2), 159-170. https://doi.org/10.24425/aoa.2023.145234

Al-Obaidi, A. R. (2024). Effect of different guide vane configurations on flow field investigation and performances of an axial pump based on CFD analysis and vibration investigation. *Experimental Techniques*, *48*(1), 69-88. https://doi.org/10.1007/s40799-023-00641-5

Al-Obaidi, A. R., & Alhamid, J. (2023). Investigation of the main flow characteristics mechanism and flow dynamics within an axial flow pump based on different transient load conditions. *Iranian Journal of Science and Technology, Transactions of Mechanical Engineering*, 1-19. https://doi.org/10.1007/s40997-022-00586-x

Al-Obaidi, A. R., & Qubian, A. (2022). Effect of outlet impeller diameter on performance prediction of centrifugal pump under single-phase and cavitation flow conditions. *International Journal of Nonlinear Sciences and Numerical Simulation*, *23*(7-8), 1203-1229. https://doi.org/10.1515/ijnsns-2020-0119

Bilus, I., & Predin, A. (2009). Numerical and experimental approach to cavitation surge obstruction in water pump. *International Journal of Numerical Methods for Heat & Fluid Flow*, *19*(7), 818-834. https://doi.org/10.1108/09615530910984091

Cao, W., Jia, Z., Zhao, Z., & Zhou, L. (2022). Validation and simulation of cavitation flow in a centrifugal pump by filter-based turbulence model. *Engineering Applications of Computational Fluid Mechanics*, *16*(1), 1724-1738. https://doi.org/10.1080/19942060.2022.2111363

Cao, W., Wang, H., Yang, X., & Leng, X. (2023). Optimization of guide vane centrifugal pumps based on response surface methodology and study of internal flow characteristics. *Journal of Marine Science and Engineering*, *11*(10), 1917. https://doi.org/10.3390/jmse11101917

Che, B., Cao, L., Chu, N., Likhachev, D., & Wu, D. (2019a). Dynamic behaviors of re-entrant jet and cavity shedding during transitional cavity oscillation on NACA0015 hydrofoil. *Journal of Fluids Engineering*, *141*(6), 061101. https://doi.org/10.1115/1.4041716

Che, B., Cao, L., Chu, N., Likhachev, D., & Wu, D. (2019b). Effect of obstacle position on attached cavitation control through response surface methodology. *Journal of Mechanical Science and Technology*, *33*, 4265-4279. https://doi.org/10.1007/s12206-019-0823-y

Che, B., Chu, N., Cao, L., Schmidt, S. J., Likhachev, D., & Wu, D. (2019c). Control effect of micro vortex generators on attached cavitation instability. *Physics of Fluids*, *31*(6). https://doi.org/10.1063/1.5099089

Cheng, W., Shao, C., & Fan, H. (2023). Impacts of cavitation on flow field distributions and pump stability in cryogenic pumps. *Journal of Low Temperature Physics*, *211*(1-2), 86-107. https://doi.org/10.1007/s10909-023-02944-8

Gu, Y., Ma, L., Yu, S., Yan, M., Wu, D., & Mou, J. (2023). Surface cavitation flow characterization of jet hydrofoils based on vortex identification method. *Physics of Fluids*, *35*(1). https://doi.org/10.1063/5.0126564

Huang, H. B., Long, Y., & Ji, B. (2020). Experimental investigation of vortex generator influences on propeller cavitation and hull pressure fluctuations. *Journal of Hydrodynamics*, *32*, 82-92. https://doi.org/10.1007/s42241-020-0005-5

Kadivar, E., el Moctar, O., & Javadi, K. (2018). Investigation of the effect of cavitation passive control on the dynamics of unsteady cloud cavitation. *Applied Mathematical Modelling*, *64*, 333-356. https://doi.org/10.1016/j.apm.2018.07.015

Kadivar, E., el Moctar, O., & Javadi, K. (2019). Stabilization of cloud cavitation instabilities using cylindrical cavitating-bubble generators (CCGs). *International Journal of Multiphase Flow*, *115*, 108-125. https://doi.org/10.1016/j.ijmultiphaseflow.2019.03.019

Kadivar, E., Timoshevskiy, M. V., Pervunin, K. S., & el Moctar, O. (2020a). Cavitation control using cylindrical cavitating-bubble generators (CCGs): Experiments on a benchmark CAV2003 hydrofoil. *International Journal of Multiphase Flow*, *125*, 103186. https://doi.org/10.1016/j.ijmultiphaseflow.2019.103186

Kadivar, E., Timoshevskiy, M. V., Pervunin, K. S., & Moctar, O. E. (2020b). Experimental and numerical study of the cavitation surge passive control around a semi-circular leading-edge flat plate. *Journal of Marine Science and Technology*, *25*, 1010-1023. https://doi.org/10.1007/s00773-019-00697-2

Long, Y., An, C., Zhu, R., & Chen, J. (2021). Research on hydrodynamics of high velocity regions in a water-jet pump based on experimental and numerical calculations at different cavitation conditions. *Physics of Fluids*, *33*(4). https://doi.org/10.1063/5.0040618

Long, Y., Han, H. Q., Ji, B., & Long, X. P. (2022). Numerical investigation of the influence of vortex generator on propeller cavitation and hull pressure fluctuation by DDES. *Journal of Hydrodynamics*, *34*(3), 444-450. https://doi.org/10.1007/s42241-022-0032-5

Qian, C., Luo, X., Yang, C., & Wang, B. (2021). Multistage pump axial force control and hydraulic performance optimization based on response surface methodology. *Journal of the Brazilian Society of Mechanical Sciences and Engineering*, *43*, 1-14. https://doi.org/10.1007/s40430-021-02849-1

Qiu, N., Zhou, W., Che, B., Wu, D., Wang, L., & Zhu, H. (2020). Effects of microvortex generators on cavitation erosion by changing periodic shedding into new structures. *Physics of Fluids*, *32*(10). https://doi.org/10.1063/5.0021162

Song, P., Wei, Z., Zhen, H., Liu, M., & Ren, J. (2022). Effects of pre-whirl and blade profile on the hydraulic and cavitation performance of a centrifugal pump. *International Journal of Multiphase Flow*, *157*, 104261. https://doi.org/10.1016/j.ijmultiphaseflow.2022.104261

Wang, C., Yao, Y., Yang, Y., Chen, X., Wang, H., Ge, J., Cao, W. & Zhang, Q. (2023). Automatic optimization of centrifugal pump for energy conservation and efficiency enhancement based on response surface methodology and computational fluid dynamics. *Engineering Applications of Computational Fluid Mechanics*, *17*(1), 2227686. https://doi.org/10.1080/19942060.2023.2227686

Yan, L., Gao, B., Ni, D., Zhang, N., & Zhou, W. (2023). Numerical analysis of the influence of the non-uniform inflow induced by streamwise vortices on the cavitating flow around hydrofoil. *Ocean Engineering*, *278*, 114324. https://doi.org/10.1016/j.oceaneng.2023.114324

Yu, A., Li, L., Zhou, D., & Ji, J. (2023). Large eddy simulation of the pulsation characteristics in the cavitating flow around a NACA0015 hydrofoil. *Ocean Engineering*, *267*,113289. https://doi.org/10.1016/j.oceaneng.2022.113289

Zhao, G., Cao, L., Che, B., Wu, R., Yang, S., & Wu, D. (2021). Towards the control of blade cavitation in a waterjet pump with inlet guide vanes: Passive control by obstacles. *Ocean Engineering*, *231*, 108820. https://doi.org/10.1016/j.oceaneng.2021.108820

Zhao, W., & Zhou, Z. (2022). Influence of geometric parameters of tiny blades on the shroud of a centrifugal pump on the cavitation suppression effect. *Frontiers in Energy Research*, *10*, 865885. https://doi.org/10.3389/fenrg.2022.865885

Zhao, Y., Li, G., Zhao, F., Wang, X., & Xu, W. (2023). Analysis of macroscopic cavitation characteristics of a self-excited oscillating cavitation jet nozzle. *Journal of Applied Fluid Mechanics*, *16*(11), 2130-2141. http://doi.org/10.47176/jafm.16.11.1923

Zhou, J., He, D., Zhang, R., & Zhao, W. (2023). Research on the performance of a centrifugal aviation fuel pump based on response surface methodology. *Processes*, *11*(11), 3055. https://doi.org/10.3390/pr11113055